Lithographically Defined Three-Dimensional Graphene Structures

Xiaoyin Xiao,[†] Thomas E. Beechem,[†] Michael T. Brumbach,[†] Timothy N. Lambert,[†] Danae J. Davis,[†] Joseph R. Michael,[†] Cody M. Washburn,[†] Joseph Wang,[‡] Susan M. Brozik,[†] David R. Wheeler,[†] D. Bruce Burckel,[†,*] and Ronen Polsky[†,*]

[†]Sandia National Laboratories, Albuquerque, New Mexico 87185, United States and [‡]Department of NanoEngineering, University of California at San Diego, La Jolla, California 92093-0448, United States

ABSTRACT

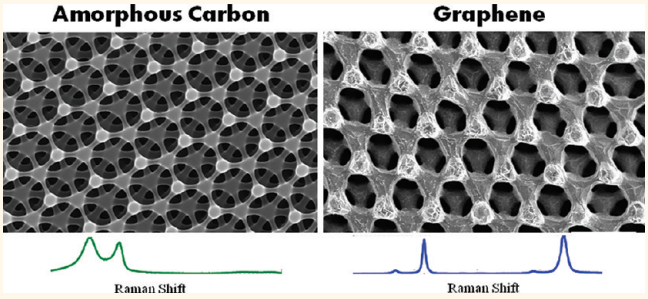

A simple and facile method to fabricate 3D graphene architectures is presented. Pyrolyzed photoresist films (PPF) can easily be patterned into a variety of 2D and 3D structures. We demonstrate how prestructured PPF can be chemically converted into hollow, interconnected 3D multilayered graphene structures having pore sizes around 500 nm. Electrodes formed from these structures exhibit excellent electrochemical properties including high surface area and steady-state mass transport profiles due to a unique combination of 3D pore structure and the intrinsic advantages of electron transport in graphene, which makes this material a promising candidate for microbattery and sensing applications.

KEYWORDS: graphene · lithography · three-dimensional · electrochemistry

The two-dimensional (2D) lattice of sp^2-bonded carbon atoms distinguishes graphene from other carbon allotropes such as graphite, diamond, and carbon nanotubes.[1] Additionally, high electron mobility provides graphene with unique electrical properties such that graphene-based devices have been proposed as possible alternatives to silicon-based ones. The optical properties of graphene have resulted in applications ranging from photoelectric devices to touch screen electronic technology.[2−4] Unlike semiconductor applications where the planar nature of the material fits well with traditional device architectures, the use of graphene for electrochemical transduction[5] and gas-phase chemical sensing[6] and as an interface for a host of biological applications[7] would ideally capitalize upon the unique "2D" properties of the material somehow translated into a "3D" architecture. This study focuses on the fabrication of such a 3D graphene material toward these ends.

There are numerous methods for the preparation of graphene. These include cleavage of highly oriented pyrolytic graphite (HOPG),[8] reduction of graphite oxide,[9] thermal decomposition of silicon carbide,[10] chemical vapor deposition (CVD),[11] and segregation by catalytic metals such as nickel and copper.[12] The Tour group has described graphene formation from encapsulating a variety of sacrificial carbon sources (such as PDMS, PMMA, and polystyrene) with nickel coatings followed by annealing that allowed carbon atoms to diffuse and order themselves into the metal catalyst film producing bilayer graphene films.[13,14] Recently, Chen *et al.* reported on the formation of a 3D macroscopic graphene structure using a template-directed CVD approach.[15] Highly interconnected 3D nickel foam was used as a scaffold to precipitate wrinkled graphene films that, after etching of the underlying nickel, produced a mechanically robust free-standing 3D graphene structure with macroscopic pore dimensions on the order of hundreds of micrometers.

Herein we describe the conversion of predefined 3D pyrolyzed photoresist films (PPF) into well-defined 3D porous graphene with dimensions 2 orders of magnitude smaller than previously reported for interconnected 3D graphene films. The conversion follows a three-step process presented in Figure 1, where 3D amorphous carbon structures are conformally sputtered with nickel and annealed, converting the material into 3D graphitic monoliths. Acidic etching removes the remaining nickel, leaving structures that are hollow and consist of

* Address correspondence to rpolsky@sandia.gov; dbburck@sandia.gov.

Received for review February 13, 2012 and accepted March 9, 2012.

Published online March 09, 2012
10.1021/nn300655c

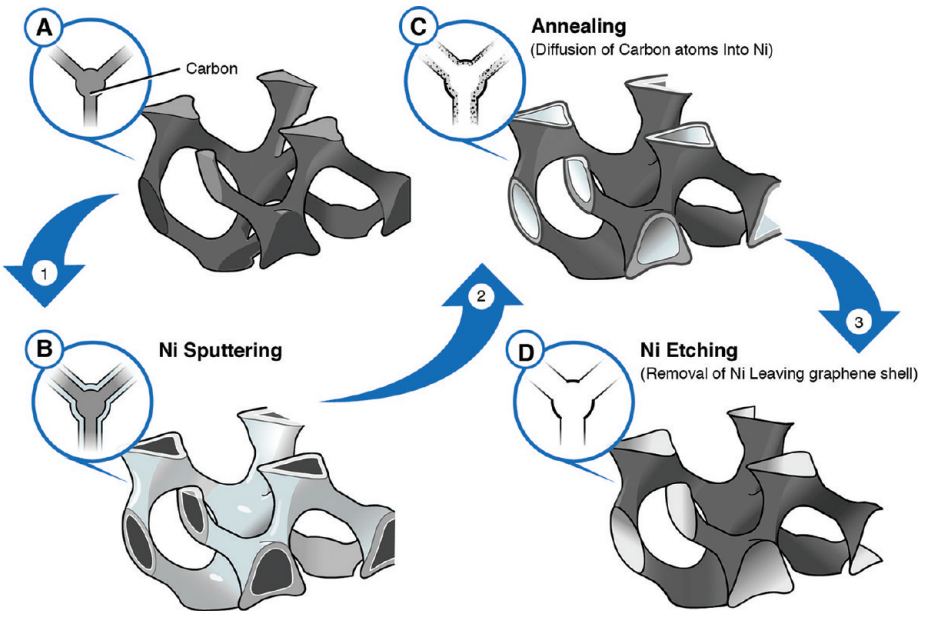

Figure 1. Schematic drawings illustrating the steps and mechanism for chemical conversion of amorphous porous carbon to 3D graphene: (A) porous carbon, (B) conformal Ni coating, (C) diffusion of carbon into Ni top surface during thermal annealing, and (D) hollow 3D graphene after Ni etching.

multilayered graphene. PPF have found use as highly versatile electrode materials that are generated by the pyrolysis of commercially available microfabrication-quality photoresist in a reducing atmosphere. The pyrolysis in a reducing atmosphere facilitates the loss of heteroatoms (N, P, O, *etc.*), leaving behind a conducting carbon surface with physical and electrochemical properties similar to glassy carbon electrodes.[16] One of the main advantages of preparing electrodes from such a technique is that the electrodes can be patterned in numerous ways. For example, 2D interdigitated arrays,[17] 3D posts,[18] carbon nanopyramids,[19] and multilayered microporous carbon structures have been reported.[20] We believe that the conversion of PPF into graphene is an intriguing and novel methodology to create 3D graphene structures using a host of already available lithographic patterning techniques. Moreover, the large concentration of catalytic edge sites implicit with a 3D multilayer graphene makes the present material particularly attractive as an electrode material applicable in energy and sensor devices.

RESULTS AND DISCUSSION

To realize such structures, interference lithography was implemented to create 3D porous carbon with approximately face-centered cubic structure as presented in Figure 2A. The structures consist of five interconnected layers with nanometer-sized carbon arms and nodes arranged in a triangular in-plane structure. Electrodes formed from this 3D porous carbon have been shown to yield increased mass transport of fuels and analytes (measured electrochemically) due to hemispherical diffusion profiles

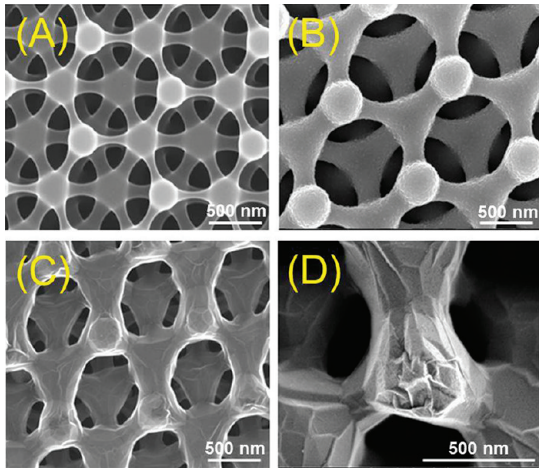

Figure 2. SEM images of porous carbon (A), porous carbon coated with nickel (B), and 3D graphene (C, D).

inside the structures.[21] At this point, the carbon composing the structure exists largely in a sp^3 form with occasional microdomains arranged in a sp^2 fashion. The conversion to graphene was accomplished by first sputtering nickel at a half angstrom per second for 20 min. Figure 2B shows a smooth coating of Ni on porous carbon before thermal annealing. The open porous configuration of these structures results in complete film coatings down to bottom layers (including undersides) after sputtering.[22] Annealing was performed at 750 °C in a 5%/95% H_2/N_2 atmosphere for 50 min, and finally the Ni layer was etched in a 2 M H_2SO_4 solution for 8 h. This process results in the formation of a 3D graphene structure. The wrinkles and ripples shown in Figure 2C and D are typical and characteristic of polycrystalline graphene structures.

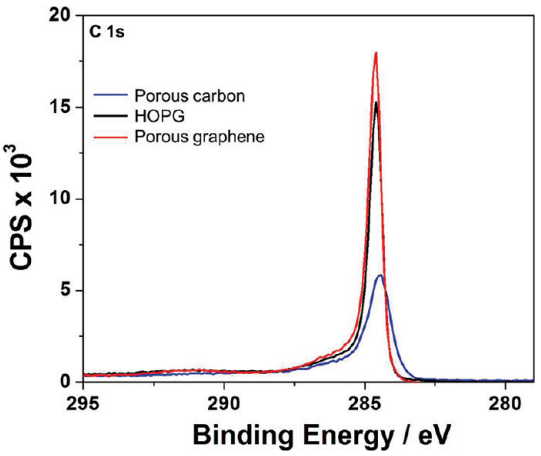

Figure 3. XPS spectra of the C 1s spectral feature for porous graphene (red), HOPG (black), and an unconverted porous carbon (blue).

Figure 3 shows the X-ray photoelectron spectroscopy (XPS) signal arising from the 3D graphene indicating a complete conversion of the predominately sp^3 porous surface to sp^2 carbon, a deduction that is based upon the nearly identical response to that of a highly ordered pyrolytic graphite standard sample. Specifically, the C 1s feature exhibits a sharp peak (fwhm ~0.5 eV) near 284.6 eV, characteristic of a nearly uniform sp^2 carbon surface with a slight tailing of intensity to higher binding energy. Graphene displays a similar C 1s peak with assignments described generally as 285.5 eV (C−C), 285.4 eV (C−H), 286.8 eV (C−O), 288.3 eV (C═O), and 290.6 eV (O−C═O and carbonate), all ±0.2 eV.[23] For comparison, the spectrum of unconverted 3D porous carbon is shown as the blue curve, exhibiting a spectrally shifted peak with lower overall intensity and larger fwhm. The preconverted porous carbon also displays trace amounts of sulfur and nitrogen, which substantially decrease after conversion to graphene, as does the O/C ratio, shown in Figure S1.

Raman spectroscopy is then utilized to determine the type of sp^2 carbon that is present, *e.g.*, graphite, graphene, or vitreous carbon. Shown in Figure 4b and c are Raman images where the color is scaled according to the intensity of the G peak and the width of the 2D mode, respectively. When comparing these to a micrograph of the same region (Figure 4a), the G peak's intensity follows the morphology of the underlying periodic three-dimensional structure, whereas the width (fwhm) of the 2D mode is largely independent of the underlying structure. The G mode's intensity variation can be viewed as a consequence of the 3D structure in which the signal is reduced for layers below the focal plane, thus giving rise to the lower response in the "holes" of the top surface. In contrast, the 2D fwhm varies in a manner that is not consistent with the morphology, as it exhibits regions of narrow line width (fwhm ~50 cm^{-1}) interspersed within areas having a much broader response (fwhm ~75 cm^{-1}). Figure 4d displays the average spectra of these areas, termed the α-region and β-regions, respectively, along with a graphite spectrum and that of the porous carbon before graphitization such that the differences in the materials might be investigated.

Most strikingly, the α-regions have an intensity ratio of the 2D to G modes that is greater than 1—*i.e.*, *I*(2D)/*I*(G) > 1—a response that is most often associated with graphene films composed of less than 5 monolayers.[24,25] To further investigate, the line shape of the regions was fit using a variable number of Lorentzian function(s). This line shape evolves as a consequence of the double-resonance phenomenon and provides direct insight into the electronic band structure and thus the type of sp^2 carbon that is present.[26] The α-region is well fit with a single Lorentzian function having a line width of 55 cm^{-1}, as is shown in Figure 4e. A single Lorentzian line shape is indicative of either turbostratic graphite,[27,28] twisted graphene,[29−31] or monolayer graphene.[32] In turbostratic graphite, the single Lorentzian response is most often accompanied by a large D-peak response,[33] a fact that is not observed here. In monolayer graphene, the fwhm is often much smaller, typically on the order of 24 cm^{-1}.[32] As the fwhm is known to broaden with increasing layer number,[33] we conclude that the α-region is most likely made up of twisted multilayer graphene. Furthermore, since the 2D intensity is greater than that of the G intensity, we further deduce that this twisted multilayer is less than 5 monolayers thick.

Within the β-region the intensity of G band is greater than that of the 2D band. Additionally, the 2D fwhm is much broader and can no longer be fit with a single Lorentzian. Instead, it necessitates three separate Lorentzian functions to fully capture the shape (see Figure 4e). The need for three different functions is in contrast to graphite, where only two Lorentzians describe the response. Such a shape has been reported previously for graphitic foams in which the complex response is attributed to a convolution of signals emanating from two (1-Lorentzian) and three (2-Lorentzian) dimensional graphite.[34] We therefore conclude that the β-region is similar in that it is a multilayer (>5 monolayers) graphite stack.

Cross sectional imaging of the 3D graphene structures is presented in Figure 5. Of particular note is that the structures appear to be hollow. It is well known that amorphous carbon can easily diffuse into Ni at elevated temperatures and concomitantly graphitize at the nickel surface.[35] The hollow nature of these structures is therefore attributed to either the complete reordering of carbon at the nickel surface or the incomplete diffusion of all carbon atoms through the Ni and their sequestration into the bulk of the Ni, which is subsequently washed away during acidic etching of the Ni according to the scheme presented in Figure 1. This explains the lack of an sp^3 carbon signature in the XPS

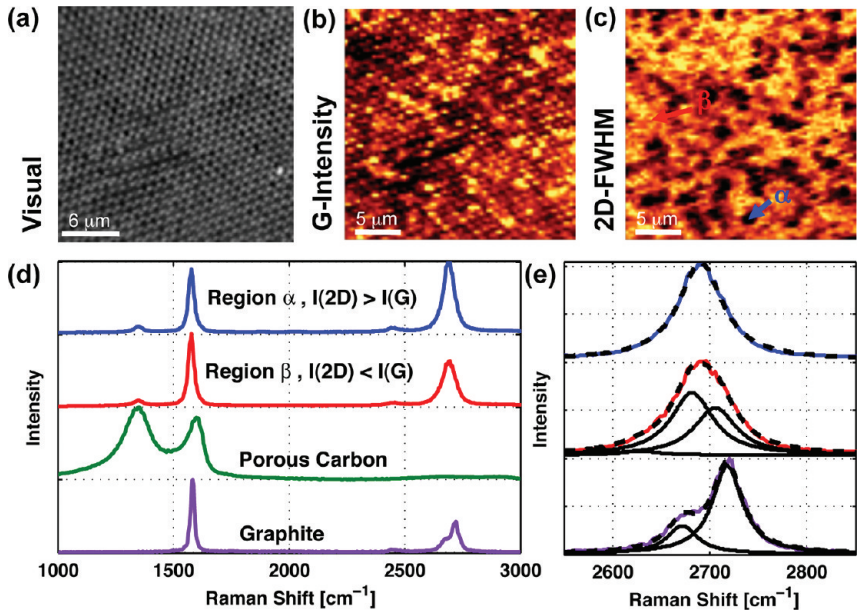

Figure 4. (a) Micrograph of analyzed area exhibiting the periodic structure. (b) Raman mapping of the G-peak intensity exhibits a response in line with the underlying microstructure shown in (a). (c) In contrast, the 2D fwhm does not follow the underlying microstructure, as differing regions having sizes greater than the periodicity are apparent. These regions exhibit markedly different spectral character, as shown by the average spectra (d) of the regions denoted α and β. Variations in the *I*(2D)/*I*(G) ratio along with the shape of the 2D fwhm indicate that the α-region is most likely a twisted multilayer graphene of less than 5 monolayers, whereas the β-region is thicker, albeit while retaining graphitic character. Color scale for total 2D fwhm in (c): dark: 48 cm^{-1}, bright: 75 cm^{-1}. (e) Lorentzian fit of G bands in regions α and β and graphite.

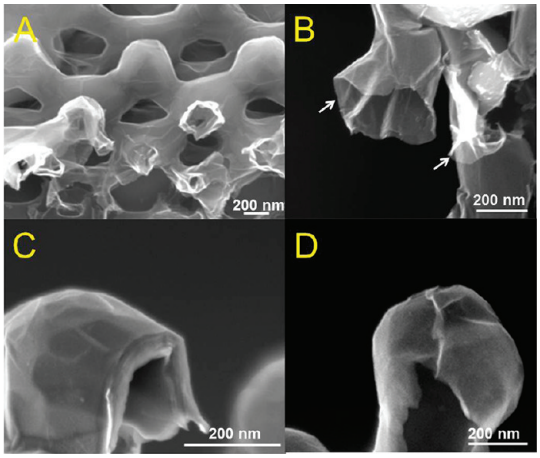

Figure 5. SEM images at the cross sections show hollow thin arms (A, B) and thick nodes (C, D). The arrows point to thin layered graphene sheets.

analysis, which one would expect if there were a non-graphene carbon core. It can be seen that the wall thickness varies from less than 5 nm at the connecting arms (Figure 5A, B) to approximately 20−30 nm at the spherical nodes (Figure 5C, D), although this approximation is difficult to quantify by SEM alone. This further supports the Raman analysis of two distinct regions having a varying thickness.

In order to assess the potential application of 3D graphene as electrodes, we investigated their electrochemical performance and compared them with the original amorphous porous carbon along with a glassy carbon electrode. Figure 6A shows the cyclic voltammetric profiles of the well-known redox mediator potassium ferricyanide. The planar glassy carbon electrodes demonstrate a scan rate dependence on current, even for modest scan rates. For the 3D graphene electrode, however, the steady-state diffusion-controlled current is maintained up to a scan rate of ~100 mV/s (flat plateau region from 5 to 100 mV/s in Figure 6B), indicative of hemispherical diffusion and enhanced mass transport.[21] As the scan rate is increased beyond this range, the oxidation/reduction waves evolve to become peak shaped for both the porous carbon and porous graphene. Interestingly, the peak separation is largely unchanged from 100 to 500 mV/s for the 3D graphene, whereas the peak separation undergoes a large shift for the porous carbon electrode (Figure 6B, inset), indicating more favorable electron transfer kinetics are occurring at the 3D graphene.

We attribute much of this behavior to the microscopically rough and crystalline graphene surface (comparing Figure 2A and C), which leads to a high density of surface states, which act as catalytic edge planes. We believe the presence of these catalytic planes coupled with the high electron conductivity associated with multilayer graphene, as compared to glassy carbon, combines to create an electrode with enhanced electron transfer processes[36] and hence better electrochemical properties. This is illustrated in Figure 6C from a direct comparison of the ferricyanide response for the 3D graphene and glassy carbon materials at 5 mV/s. Of note is the ~20 mV negative shift in half-wave peak potential being observed

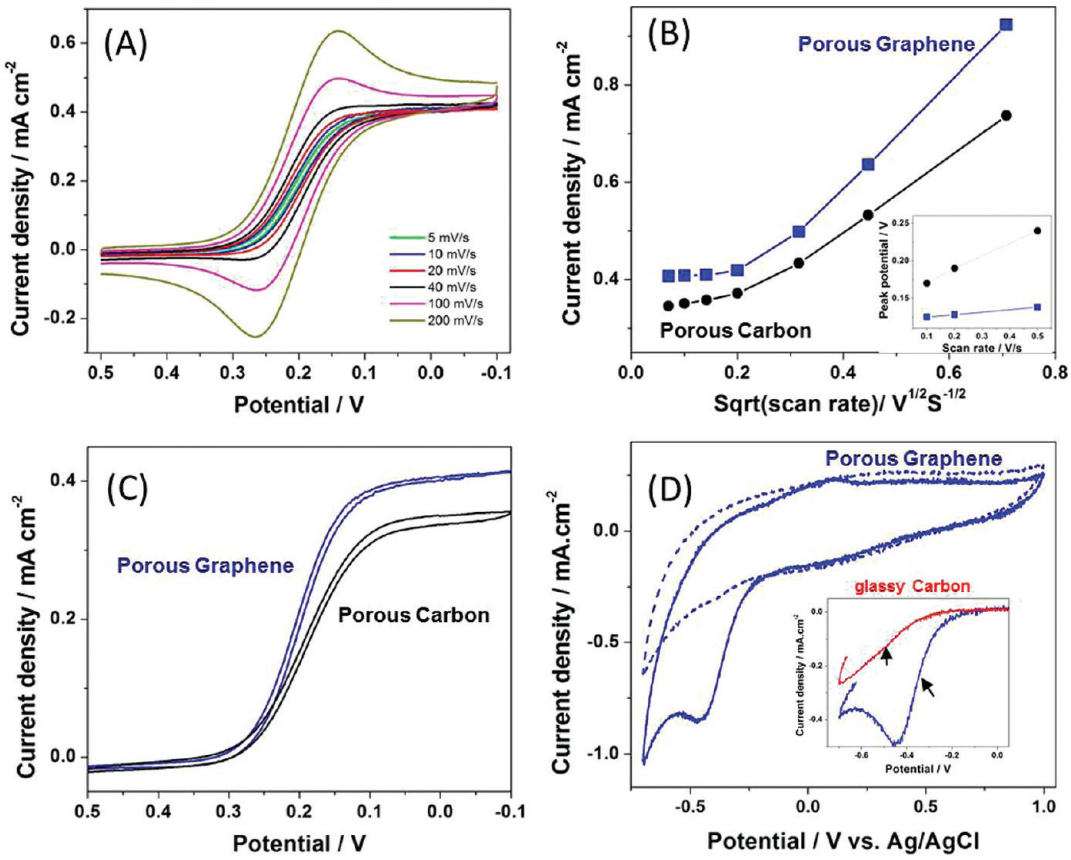

Figure 6. (A) Cyclic voltammograms of a 3D graphene in 2 mM $K_3Fe(CN)_6$ + 100 mM KCl from 5 to 200 mV/s. Surface area: 0.14 cm^2. (B) Current *versus* square root of scan rate illustrating the diffusion-controlled steady state to kinetic process (inset, peak potential *versus* scan rate). (C) Voltammetric curves compared between porous graphene and porous carbon at 5 mV/s. (D) Oxygen reduction at 3D graphene in oxygen-saturated (solid curve) and nitrogen-saturated (dashed line) 0.5 M H_2SO_4, 100 mV/s (inset, comparison between 3D graphene (blue curve) and glassy carbon (red curve) after background subtraction).

for the 3D graphene.[37,38] The increase from both mass and charge transport is essential to achieve highly catalytic surfaces. Figure 6D shows that the current from oxygen reduction is significantly larger than at the glassy carbon electrode and original porous carbon (Figure S3). Although the onset potentials for oxygen reduction at these three electrodes are nearly the same, the half-wave potential at the porous graphene is significantly more positive, at around −0.34 V in comparison to −0.51 V at glassy carbon. This again demonstrates that a faster electron transfer process occurs at the 3D graphene and also its possible utility as a fuel cell cathode.

CONCLUSIONS

In summary, we have demonstrated a route to production of robust 3D graphene electrodes having pore sizes on the order of 500 nm, which we believe to be the lowest dimensions reported to date. These electrodes exhibit superior electrochemical behavior compared to 3D porous carbon and planar glassy carbon electrodes. XPS and Raman analysis confirm the complete conversion of the sp^3-dominated carbon to sp^2 carbon after the chemical conversion. The combination of the intrinsically high electron conductivity of graphene, the high density of catalytic edge planes, and the increased mass transport behavior inherent with the geometry of the 3D micrometer scale structuring results in a promising new electrode material. Furthermore, the versatility in patterning PPF combined with its conversion to graphene should open a host of possibilities for new 3D graphene architecture.

METHODS

Scanning electron microscope (SEM) imaging was performed on a Zeiss Supra 55VP field emission gun scanning electron microscope or an FEI Magellan 400 SEM. Raman spectroscopy was performed on an alpha 300R confocal microscope (WiTec GmBh) using 532 nm incident radiation focused to a spot size of 700 nm. For Raman imaging, a 25 × 25 μm region was analyzed by acquiring a spectrum every 333 nm. The spectral resolution of the system is ~1 cm^{-1}. Electrochemical measurements for the ferricyanide studies were performed on a CH Instruments 660 electrochemical analyzer (Austin, TX, USA), while oxygen reduction studies were performed on a VoltaLab PGZ100 All-In-One potentiostat. All electrochemical experiments were *versus* a

Pt counter and Ag/AgCl in 3 M NaCl reference from Bioanalytical Systems (West Lafayette, IN, USA).

Interferometric Lithography of 3D Porous Carbon Electrodes. A bottom antireflection coating, iCON-7 (Brewer Science, Rolla, MO, USA), was spun onto silicon wafers at 3000 rpm and baked on a vacuum hot plate at 205 °C for 60 s. Negative tone NR7 from Futurrex Inc. was used in all of the experiments. A thin layer of NR 7 100P (~100 nm) was deposited and spun at 3000 rpm to create an adhesion layer. After flood exposure and post-exposure bake at 130 °C on a vacuum hot plate, a thick layer (6 μm) of NR7-6000P was deposited and spun at 3000 rpm and soft-baked at 130 °C. The frequency-tripled 355 nm line of a Q-switched Nd:YAG laser was used to form the interference pattern. The beam was expanded and split into two separate beams and interfered with an angle of 32° between the plane-wave propagation vectors. The plane of incidence contains both propagation vectors as well as the angle bisector of the propagation vectors, which is tilted with respect to the sample surface normal by 45°. After each exposure the sample is rotated in the plane by 120° and the process is repeated a total of three times. After exposure the sample received a post-exposure bake of 85 °C for 2 min on the vacuum hot plate. A 120 s puddle development using RD-6 (Futurrex, Inc.) and spin drying completed fabrication of the resist structures. The samples were baked on a hot plate at 180 °C for 30 min. The samples were then pyrolyzed at 1100 °C for 1 h in forming gas (5% H_2 and 95% N_2). Substrates were rinsed with 2-propanol and water before use.

Conflict of Interest: The authors declare no competing financial interest.

Acknowledgment. We would like to acknowledge Christopher Brigman for graphics construction. Sandia is a multiprogram laboratory operated by Sandia Corporation, a Lockheed Martin Company, for the United Stated Department of Energy's National Nuclear Security Administration under Contract DE-AC04-94AL85000. The authors acknowledge the Sandia National Laboratories' Laboratory Directed Research & Development (LDRD).

Supporting Information Available: Supplemental results. This material is available free of charge *via* the Internet at http://pubs.acs.org.

REFERENCES AND NOTES

1. Geim, A. K.; Novoselov, K. S. The Rise of Graphene. *Nat. Mater.* **2007**, *6*, 183–191.
2. Mayorov, A. S.; Elias, D. C.; Mucha-Kruczynski, M.; Gorbachev, R. V.; Tudorovskiy, T.; Zhukov, T.; Morozov, S. V.; Katsnelson, M. I.; Falko, V. I.; Geim, A. K.; Novoselov, K. S. Interaction-Driven Spectrum Reconstitution in Bilayer Graphene. *Science* **2011**, *333*, 860–863.
3. Liao, L.; Lin, Y. C.; Bao, M.; Cheng, R.; Bai, J.; Liu, Y.; Qu, Y.; Wang, K. L.; Huang, Y.; Duan, X. High-Speed Graphene Transistors with a Self-Aligned Nanowire Gate. *Nature* **2010**, *467*, 305–308.
4. Cao, H.; Yu, Q.; Jauregui, L. A.; Tian, J.; Wu, W.; Liu, Z.; Jalilian, R.; Benjamin, D. K.; Jiang, Z.; Bao, J.; Pei, S. S.; Chen, Y. P. Electronic Transport in Chemical Vapor Deposited Graphene Synthesized on Cu: Quantum Hall Effect and Weak Localization. *Appl. Phys. Lett.* **2010**, *96*, 122106–122109.
5. Goh, M. S.; Pumera, M. The Electrochemical Response of Graphene Sheets Is Independent of the Number of Layers from a Single Graphene Sheet to Multilayer Stacked Graphene Platelets. *Chem. Asian J.* **2010**, *2*, 2355–2357.
6. Lu, G.; Park, S.; Yu, K.; Ruoff, R.; Ocola, L. E.; Rosenmann, D.; Chen, J. Toward Practical Gas Sensing with Highly Reduced Graphene Oxide: A New Signal Processing method to Circumvent Run-to-Run and Device-to-Device Variations. *ACS Nano* **2011**, *5*, 1154–1164.
7. Garaj, S.; Hubbard, W.; Reina, A.; Kong, J.; Branton, D.; Golovchenko, J. A. Graphene as a Subnanometre Trans-electrode Membrane. *Nature* **2010**, *467*, 190–193.
8. Li, D.; Kaner, R. B. Graphene-Based Materials. *Science* **2008**, *320*, 1170–1171.
9. Zhu, Y. Z.; Stoller, M. D.; Cai, W.; Velamakanni, A.; Piner, R. D.; Chen, D.; Ruoff, R. S. Exfoliation of Graphite Oxide in Propylene Carbonate and thermal Reduction of the Resulting Graphene Oxide Platelets. *ACS Nano* **2010**, *4*, 1227–1233.
10. Aristov, V. Y.; Urbanik, G.; Kummer, K.; Vyalikh, D. V.; Molodtsova, O. V.; Preobrajenski, A. B.; Zakharov, A. A.; Hess, C.; Hanje, T.; *et al.* Graphene Synthesis on Cubic SiC/Si Wafers. Perspectives for Mass Production of Graphene-Based Electronic Devices. *Nano Lett.* **2010**, *10*, 992–005.
11. Obraztsov, A. N. Chemical Vapour Deposition: Making Graphene on a Large Scale. *Nat. Nanotechnol.* **2009**, *4*, 212–213.
12. Liu, N.; Fu, L.; Dai, B.; Yan, K.; Liu, X.; Zhao, R.; Zhang, Y.; Liu, Z. Universal Segregation Growth Approach to Wafer-Size Graphene from Non-Noble Metals. *Nano Lett.* **2011**, *11*, 297–303.
13. Yan, Z.; Peng, Z.; Sun, Z.; Yao, J.; Zhu, Y.; Liu, Z.; Ajayan, P. M.; Tour, J. M. Growth of Bilayer Graphene on Insulating Substrates. *ACS Nano* **2011**, *5*, 8187–8192.
14. Peng, Z.; Yan, Z.; Sun, Z.; Tour, J. M. Direct Growth of Bilayer Graphene on SiO_2 Substrates by Carbon Diffusion through Nickel. *ACS Nano* **2011**, *5*, 8241–8247.
15. Chen, Z.; Ren, W.; Gao, L.; Pei, S.; Cheng, H. M. Three-Dimensional Flexible and Conductive Interconnected Graphene Networks Grown by Chemical Vapour Deposition. *Nat. Mat.* **2011**, *10*, 424–428.
16. McCreery, R. L. Advanced Carbon Electrode Materials for Molecular Electrochemistry. *Chem. Rev.* **2008**, *108*, 2646–2687.
17. Raganathan, S.; McCreery, R. L. Electroanalytical Performance of Carbon Films with Near-Atomic Flatness. *Anal. Chem.* **2011**, *73*, 893–900.
18. Wang, C.; Jia, G.; Taherabadi, L. H.; Madou, M. J. A Novel Method for the Fabrication of High-Aspect Ratio C-MEMS Structures. *J. Microelectromech. Syst.* **2005**, *14*, 348–358.
19. Polsky, R.; Washburn, C. M.; Montano, G. M.; Liu, H.; Edwards, T. L.; Lopez, D. M.; Harper, J. C.; Brozik, S. M.; Wheeler, D. R. Reactive Ion Etching of Gold-Nanoparticle-Modified Pyrolyzed Photoresist Films. *Small* **2009**, *5*, 2510–2513.
20. Burckel, D. B.; Washburn, C. M.; Raub, A. K.; Brueck, S. R. J.; Wheeler, D. R.; Brozik, S. M.; Polsky, R. Lithographically Defined Porous Carbon Electrodes. *Small* **2009**, *5*, 2792–2796.
21. Xiao, X.; Roberts, M. E.; Wheeler, D. R.; Washburn, C. M.; Edwards, T. L.; Brozik, S. M.; Montano, G. A.; Bunker, B. C.; Burckel, D. B.; Polsky, R. Increased Mass Transport at Lithographically Defined 3-D Porous Carbon Electrodes. *ACS Appl. Mater. Interfaces* **2010**, *2*, 3179–3184.
22. Xiao, X.; Nogan, J.; Beechem, T.; Montano, G. A.; Washburn, C. M.; Wang, J.; Brozik, S. M.; Wheeler, D. R.; Burckel, D. B.; Polsky, R. Lithographically-Defined 3D Porous Networks as Active Substrates for Surface Enhanced Raman Scattering. *Chem. Commun.* **2011**, *47*, 9858–9860.
23. Lambert, T. L.; Chavez, C. A.; Bell, N. S.; Washburn, C. M.; Wheeler, D. R.; Brumbach, M. T. Large Area Mosaic Films of Graphene-Titania: Self Assembly at the Liquid-Air Interface and Photoresponsive Behavior. *Nanoscale* **2011**, *3*, 188–191.
24. Ferrari, A. C.; Meyer, J. C.; Scardaci, V.; Casiraghi, C.; Lazzeri, M.; Mauri, F.; Piscanec, S.; Jiang, D.; Novoselov, K. S.; Roth, S.; Geim, A. K. Raman Spectrum of Graphene and Graphene Layers. *Phys. Rev. Lett.* **2006**, *97*, 187401–187404.
25. Gupta, A.; Chen, G.; Joshi, P.; Tadigadapa, S.; Eklund, P. C. Raman Scattering from High-Frequency Phonons in Supported n-Graphene Layer Films. *Nano Lett.* **2006**, *6*, 2667–2673.
26. Reich, S.; Thomsen, C. Raman Spectroscopy of Graphite. *Philos. Trans. R. Soc., A* **2004**, *362*, 2271–2288.
27. Ferrari, A. Raman Spectroscopy of Graphene and Graphite: Disorder, Electron−Phonon Coupling, Doping and Non-adiabatic Effects. *Solid State Commun.* **2007**, *143*, 47–57.
28. Pimenta, M.; Dresselhaus, G.; Dresselhaus, M.; Cancado, L.; Jorio, A.; Saito, R. Studying Disorder in Graphite-Based

Systems by Raman Spectroscopy. *Phys. Chem. Chem. Phys.* **2007**, *9*, 1276–1290.
29. Poncharal, P.; Ayari, A.; Michel, T. J.; Sauvajol, L. Raman Spectra of Misoriented Bilayer Graphene. *Phys. Rev. B* **2008**, *78*, 113407.
30. Ni, Z.; Wang, Y.; Yu, T.; You, Y.; Shen, Z. Reduction of Fermi Velocity in Folded Graphene Observed by Resonance Raman Spectroscopy. *Phys. Rev. B* **2008**, *77*, 235403.
31. Ohta, T.; Beechem, T. E.; Robinson, J. T.; Kellogg, G. L. Long-Range Atomic Ordering and Variable Interlayer Interactions in Two Overlapping Graphene Lattices with Stacking Misorientations. *Phys. Rev. [Sect.] B* **2012**, *85*, 075415.
32. Malard, L.; Pimenta, M.; Dresselhaus, G.; Dresselhaus, M. Raman Spectroscopy in Graphene. *Phys. Rep.* **2009**, *473*, 51–87.
33. Lee, D.; Riedl, C.; Krauss, B.; von Klitzing, K.; Starke, U.; Smet, J. Raman Spectra of Epitaxial Graphene on SiC and of Epitaxial Graphene Transferred to SiO_2. *Nano Lett.* **2008**, *8*, 4320–4325.
34. Barros, E. B.; Demir, N. S.; Souza Filho, A. G.; Mendes Filho, J.; Jorio, A.; Dresselhaus, G.; Dresselhaus, M. S. Raman Spectroscopy of Graphitic Foams. *Phys. Rev. B* **2005**, *71*, 165422.
35. Anton, R. On the Reaction Kinetics of Ni with Amorphous Carbon. *Carbon* **2008**, *46*, 656–662.
36. Li., W.; Tan, C.; Lowe, M. A.; Abruna, H.; Ralph, D. C. Electrochemistry of Individual Monolayer Graphene Sheets. *ACS Nano* **2011**, *5*, 2264–2270.
37. Mirkin, M. V.; Bard, A. J. Simple Analysis of Quasi-Reversible Steady-State Voltammograms. *Anal. Chem.* **1992**, *64*, 2293–2302.
38. Winkler, K. The Kinetics of Electron Transfer in Redox System on Platinum Standard-Size and Ultramicroelectrodes. *J. Electroanal. Chem.* **1995**, *388*, 151–159.